

Lognormal property of weak lensing fields

Atsushi Taruya

*Research Center for the Early Universe (RESCEU), School of Science,
University of Tokyo, Tokyo 113-0033, Japan*

ataruya@utap.phys.s.u-tokyo.ac.jp

Masahiro Takada¹, Takashi Hamana

National Astronomical Observatory, Mitaka, Tokyo 181-8588, Japan

mtakada@th.nao.ac.jp, hamana@yukawa.kyoto-u.ac.jp

Issha Kayo

Department of Physics, School of Science, University of Tokyo, Tokyo 113-0033, Japan

kayo@utap.phys.s.u-tokyo.ac.jp

and

Toshifumi Futamase

Astronomical Institute, Tohoku University, Sendai 980-8578, Japan

tof@astr.tohoku.ac.jp

ABSTRACT

The statistical property of the weak lensing fields is studied quantitatively using the ray-tracing simulations. Motivated by the empirical lognormal model that characterizes the probability distribution function of the three-dimensional mass distribution excellently, we critically investigate the validity of lognormal model in the weak lensing statistics. Assuming that the convergence field, κ ,

¹Present address: Department of Physics & Astronomy, University of Pennsylvania, PA 19104, USA; mtakada@hep.upenn.edu

is approximately described by the lognormal distribution, we present analytic formulae of convergence for the one-point probability distribution function (PDF) and the Minkowski functionals. The validity of lognormal models is checked in detail by comparing those predictions with ray-tracing simulations in various cold dark matter models. We find that the one-point lognormal PDF can describe the non-Gaussian tails of convergence fields accurately up to $\nu \sim 10$, where ν is the level threshold given by $\nu \equiv \kappa / \langle \kappa^2 \rangle^{1/2}$, although the systematic deviation from lognormal prediction becomes manifest at higher source redshift and larger smoothing scales. The lognormal formulae for Minkowski functionals also fit to the simulation results when the source redshift is low, $z_s = 1$. Accuracy of the lognormal-fit remains good even at the small angular scales $2' \lesssim \theta \lesssim 4'$, where the perturbation formulae by Edgeworth expansion break down. On the other hand, the lognormal model enables us to predict the higher-order moments, i.e., skewness, $S_{3,\kappa}$ and kurtosis, $S_{4,\kappa}$, and we thus discuss the consistency by comparing the predictions with the simulation results. Since these statistics are very sensitive to the high(low)-convergence tails, the lognormal prediction does not provide a quantitative successful fit. We therefore conclude that the empirical lognormal model of the convergence field is safely applicable as a useful cosmological tool, as long as we are concerned with the non-Gaussianity of $\nu \lesssim 5$ for low- z_s samples.

Subject headings: cosmology: theory — gravitational lensing — large-scale structure of universe — methods: numerical

1. Introduction

Cosmic shear, coherent distortions in galaxy images caused by the gravitational field of the intervening large-scale structure, has now been recognized as a powerful cosmological tool (see Mellier 1999 and Bartelmann & Schneider 2001 for reviews). Since the signal of cosmic shear reflects the gravitational potential of the total mass distribution, the cosmic shear can be a direct probe of the dark matter distribution as well as a way to measure the cosmological parameters. Recently, measurements of the cosmic shear have been independently performed by several groups (Van Waerbeke et al. 2000a; Wittman et al. 2000; Bacon, Refregier & Ellis 2000; Kaiser, Wilson & Luppino 2000; Maoli et al. 2001; Rhodes et al. 2001; van Waerbeke et al. 2001a). The estimated shear variance from the different observational data set quantitatively reconciles with each other, which is in good agreement with theoretical predictions based on the cluster normalized cold dark matter (CDM) model of structure

formation. Ongoing and future wide-field surveys using high-resolution CCD camera will promise to dramatically improve the signal-to-noise ratio of the weak lensing signals. Hence, a detail understanding of the weak lensing statistics will be necessary to extract all the cosmological information present in the data.

Of course, simplest but useful statistical measure of the weak lensing field is popular two-point statistics (Blandford et al. 1991; Miralda-Escude 1991; Kaiser 1992), however, a more clear discriminator is needed to break the degeneracy in constraining the cosmological parameters. In this respect, the non-Gaussian features of weak lensing field can be very sensitive to the density of universe and the higher-order statistics such as the skewness of local convergence field are expected to constrain the density parameter Ω_0 and even to the cosmological constant λ_0 (Bernardeau, Van Waerbeke & Mellier 1997; Jain & Seljak 1997; Van Waerbeke et al. 2001b). On the other hand, topological analysis using the Minkowski functionals of the convergence field has been proposed by Sato, Takada, Jing & Futamase (2001) in order to extract the non-Gaussian features (see also Matsubara & Jain 2001). Unfortunately, their methodology heavily relies on the validity of the perturbation theory of structure formation and cannot be applied to the weak lensing field at small angular scales $\theta \lesssim 4'$, where the underlying three-dimensional mass distribution is in the highly nonlinear regime. While the non-Gaussian signature of weak lensing fields becomes easily measurable on small scales, the non-Gaussian signal primarily reflects the nonlinear growth of the density fields, which strongly depends on the dark matter clustering properties. It is therefore desirable to investigate the statistical properties of three-dimensional mass density and explore the relation between mass distribution and weak lensing field.

Very recently, Kayo, Taruya & Suto (2001) performed a detailed analysis of the one- and two-point statistics of the three-dimensional mass distribution using the high-resolution N-body simulations. They found that the lognormal models of one- and two-point probability distribution functions (PDF) can provide an excellent approximation to the nonlinear mass distribution with Gaussian initial condition, irrespective of the shape of the initial power spectrum. The lognormal distribution has been long known as an empirical prescription characterizing the dark matter distribution and/or the observed galaxies (e.g., Hamilton 1985; Bouchet et al. 1993; Coles & Jones 1991; Kofman et al. 1994), however, there exists no rigorous explanation for its physical origin. Nevertheless, the lognormal model is now widely utilized in the astrophysical context such as analytical modeling of dark halo biasing and Ly- α forest (e.g., Mo & White 1996; Taruya & Suto 2000; Bi & Davidsen 1997). In this regard, the result of Kayo et al. (2001) is interesting and can be useful in quantifying the dark matter distribution. Furthermore, their results indicate that the lognormal distribution can also describe the weak lensing field, since the weak lensing effect primarily reflects the clustering property of dark matter distributions. Then, crucial but fundamental questions

arise as follows. How does the lognormal property emerge in the weak lensing field? Can the lognormal model provide an approximate and reliable prescription for the weak lensing statistics?

In this paper, we quantitatively investigate those issues using the ray-tracing simulations. We first consider how the statistical feature of three-dimensional mass distribution is related to that of the local convergence, i.e, the two-dimensional projected density field. Assuming that the convergence field is well-approximated by the lognormal distribution, we derive analytic formulae for the one-point PDF and the Minkowski functionals. We then perform quantitative comparisons between the lognormal models and the results of ray-tracing simulations. Furthermore, we discuss the consistency of the lognormal model with the higher-order statistics on which the previous works have mainly focused.

The plan of paper is as follows. In section 2, we briefly describe the basic definitions of weak lenses. Then, we discuss the statistical relations between mass density field and convergence field in section 3. The analytic expressions for the one-point PDF and the Minkowski functionals are presented. In section 4, the detailed comparison between the lognormal predictions and the ray-tracing simulations is described. The consistency between lognormal model and previous study is discussed in section 5. Finally, section 6 is devoted to conclusions and discussion.

2. Preliminaries

Inhomogeneous mass distribution of the large-scale structure deflects the light ray trajectory emitted from an angular direction $\boldsymbol{\theta}$ in the source plane by a small angle $\delta\boldsymbol{\theta}$ in the image plane. The differences between the deflection angles of light rays emitted from a galaxy thus induce a distortion of the galaxy image characterized by the following symmetric matrix:

$$\Phi_{i,j} \equiv \frac{\partial\delta\theta_i}{\partial\theta_j} = -2 \int_0^{\chi_s} d\chi \frac{r(\chi)r(\chi_s - \chi)}{r(\chi_s)} \partial_i\partial_j\phi(\chi), \quad (i, j = 1, 2), \quad (1)$$

where ∂_i represents a derivative with respect to θ_i , and ϕ is the gravitational potential of the three-dimensional mass density field. The variable χ_s means the quantity χ at the source redshift, and the quantities χ and $r(\chi)$ respectively denote the comoving parts of the radial and the angular-diameter distance:

$$\chi(z) = \int_0^z \frac{c dz'}{H(z')} ; \quad H(z) = H_0 \sqrt{\Omega_0(1+z)^3 + (1 - \Omega_0 - \lambda_0)(1+z)^2 + \lambda_0}, \quad (2)$$

and

$$r(\chi) = \begin{cases} \sin(\sqrt{K}\chi)/\sqrt{K} & (K > 0) \\ \chi & (K = 0) \\ \sinh(\sqrt{-K}\chi)/\sqrt{-K} & (K < 0) \end{cases} \quad (3)$$

with the quantity K being the spatial curvature of the universe, $K = (H_0/c)^2(\Omega_0 + \lambda_0 - 1)$. The matrix $\Phi_{i,j}$ is usually decomposed into the trace part, i.e, the convergence field κ_θ and the tidal shear components γ_θ defined by

$$\kappa_\theta = -\frac{1}{2}(\Phi_{1,1} + \Phi_{2,2}), \quad (4)$$

$$\gamma_\theta = -\frac{1}{2}(\Phi_{1,1} - \Phi_{2,2}) - i\Phi_{1,2}. \quad (5)$$

The shear field γ_θ can be directly estimated from the observed ellipticity of the galaxy images. The convergence field κ_θ can be then reconstructed from the shear map from the relations (4) and (5) (e.g., Kaiser & Squires 1993). Since we are interested in the *statistical* properties of the weak lensing fields, one can safely employ the Born approximation, where the quantity $\partial_i\partial_j\phi(\chi)$ are computed along the unperturbed photon trajectory (Blandford et al. 1991; Miralda-Escude 1991; Kaiser 1992). From equations (1) and (4), the convergence field along a line-of-sight is simply expressed as a weighted projection of the mass density fluctuation field δ (e.g, Mellier 1999; Bartelmann & Schneider 2001 for reviews):

$$\kappa_\theta(\boldsymbol{\theta}) = \int_0^{\chi_s} d\chi w(\chi, \chi_s) \delta[r(\chi)\boldsymbol{\theta}, \chi], \quad (6)$$

where the weight function $w(\chi, \chi_s)$ is

$$w(\chi, \chi_s) = \frac{3}{2} \left(\frac{H_0}{c} \right)^2 (1+z) \Omega_0 \frac{r(\chi)r(\chi_s - \chi)}{r(\chi_s)}. \quad (7)$$

Note that, even in the weak lensing limit, the density fluctuation δ is not small but can become much larger than unity.

In statistical analysis of weak lensing fields, the smoothing filter is practically used in order to reduce the noise due to the intrinsic ellipticity of galaxies. Throughout this paper, we adopt the top-hat smoothing function. The variance of the local convergence can then be expressed as

$$\langle \kappa^2 \rangle = \int_0^{\chi_s} d\chi [w(\chi, \chi_s)]^2 \int \frac{d^2\mathbf{k}_\perp}{(2\pi)^2} P_{\text{mass}}(k_\perp) \hat{W}_{\text{TH}}^2(k_\perp r(\chi)\theta_{\text{TH}}), \quad (8)$$

where $P_{\text{mass}}(k)$ is the three-dimensional power spectrum of the mass distribution and the function $\hat{W}_{\text{TH}}(x)$ represents the Fourier transform of the top-hat smoothing kernel:

$$\hat{W}_{\text{TH}}(x) = 2 \frac{J_1(x)}{x}. \quad (9)$$

Note that equation (8) is derived by employing the Limber’s equation (Kaiser 1992). Similarly, variance of the gradient field, $\langle(\nabla\kappa)^2\rangle$, can be expressed as

$$\langle(\nabla\kappa)^2\rangle = \int_0^{\chi_s} d\chi [w(\chi, \chi_s)]^2 r^2(\chi) \int \frac{d^2\mathbf{k}_\perp}{(2\pi)^2} k_\perp^2 P_{\text{mass}}(k_\perp) \hat{W}_{\text{TH}}^2(k_\perp r(\chi)\theta_{\text{TH}}). \quad (10)$$

Equations (8) and (10) are valid on relevant angular scales we are interested in, where the small-angle approximation holds with good accuracy (Hu 2001).

3. Lognormal model prescription

3.1. One-point PDF

The expression (6) gives a simple interpretation that the statistical feature of κ is closely related to that of the underlying density field δ . To show this more explicitly, we consider the one-point PDF, which can be constructed from a full set of the moments. Let us write down the PDF of the mass density field δ :

$$P(\delta)d\delta = \int_{-\infty}^{+\infty} \frac{dx}{2\pi\sigma^2} e^{-ix(\delta/\sigma)+\varphi_\delta(x)/\sigma^2} d\delta, \quad (11)$$

where σ denotes the root-mean-square (RMS) of δ , $\sigma = \langle\delta^2\rangle^{1/2}$ and $\varphi_\delta(x)$ means cumulant generating function:

$$\varphi_\delta(x) = \sum_{n=2}^{\infty} \frac{S_{n,\delta}}{n!} (ix)^n; \quad S_{n,\delta} \equiv \frac{\langle\delta^n\rangle_c}{\langle\delta^2\rangle^{n-1}}. \quad (12)$$

Similarly, the one-point PDF of the local convergence is written as

$$P(\hat{\kappa})d\hat{\kappa} = \int_{-\infty}^{+\infty} \frac{dx}{2\pi\langle\hat{\kappa}^2\rangle} e^{-ix(\hat{\kappa}/\langle\hat{\kappa}^2\rangle^{1/2})+\varphi_{\hat{\kappa}}(x)/\langle\hat{\kappa}^2\rangle} d\hat{\kappa}, \quad (13)$$

with the cumulant generating function for $\hat{\kappa}$, $\varphi_{\hat{\kappa}}(x)$. Here we have introduced the normalized convergence field, $\hat{\kappa} \equiv \kappa/|\kappa_{\text{min}}|$ so as to satisfy the range of the definition being $-1 < \hat{\kappa} < +\infty$. The quantity κ_{min} denotes the minimum value of the convergence field. Note that the actual value of κ_{min} in the universe should, in principle, depend on the nature of dark matter between the source galaxies and observer (Metcalf & Silk 1999; Seljak & Holtz 1999). If the dark matter is composed of a compact object such as the primordial black holes, κ_{min} might correspond to the convergence evaluated along an empty beam (see eq.[31]). On the other hand, when the dark matter is composed of a smooth microscopic component as is suggested by the standard CDM scenarios, κ_{min} becomes larger than the empty-beam value for relevant smoothing scales (see also Jain, Seljak & White 1999). As will be discussed later in section

4.2, κ_{\min} is an important quantity in controlling the lognormal model and is sensitive to the cosmological model.

Even though we have the simple relation (6) between δ and κ , the relation between the cumulant generating functions of φ_δ and $\varphi_{\hat{\kappa}}$ is practically intractable without recourse to some assumptions or approximations. Under the hierarchical ansatz for the higher order moments of δ , i.e., $S_{n,\delta} = \text{const.}$, Munshi & Jain (2000) and Valageas (2000) showed that the relation between φ_δ and $\varphi_{\hat{\kappa}}$ is greatly reduced and is expressed in a compact form:

$$\varphi_{\hat{\kappa}}(x) = \int_0^{\chi_s} d\chi \frac{\langle \hat{\kappa}^2 \rangle}{I_\kappa(\theta)} \varphi_\delta \left(\frac{w(\chi, \chi_s)}{|\kappa_{\min}|} \frac{I_\kappa(\theta)}{\langle \hat{\kappa}^2 \rangle} x \right), \quad (14)$$

where the quantity I_κ is defined by

$$I_\kappa(\theta) = \int \frac{d^2 \mathbf{k}_\perp}{(2\pi)^2} P_{\text{mass}}(k_\perp) \hat{W}_{\text{TH}}^2(k_\perp r(\chi)\theta). \quad (15)$$

This is valid as long as the small-angle approximation holds. As also proposed by those authors, since the factor $w I_\kappa / (|\kappa_{\min}| \langle \hat{\kappa}^2 \rangle)$ in equation (14) has typical values of order unity, one might use a simple approximation

$$\varphi_{\hat{\kappa}}(x) \simeq \varphi_\delta(x). \quad (16)$$

It is easy to check that this approximation holds for the limit of $z_s \rightarrow 0$, where the both quantities $w I_\kappa / (|\kappa_{\min}| \langle \hat{\kappa}^2 \rangle)$ and $\int d\chi \langle \hat{\kappa}^2 \rangle / I_\kappa(\theta)$ approach unity.

Once equation (16) is given, PDF of the convergence field, $P(\kappa)$, can be *directly* calculated from the one-point PDF of the three-dimensional mass density field $P(\delta)$, irrespective of the projection effect (see eq.[6]):

$$P(\kappa) d\kappa = P \left(\delta \rightarrow \frac{\kappa}{|\kappa_{\min}|}; \sigma \rightarrow \frac{\langle \kappa^2 \rangle^{1/2}}{|\kappa_{\min}|} \right) \frac{d\kappa}{|\kappa_{\min}|} \quad (17)$$

Now, let us recall the empirical fact that the PDF of local density $P(\delta)$ is approximately described by the lognormal distribution:

$$P_{\ln}(\delta) d\delta = \frac{1}{\sqrt{2\pi \ln(1 + \sigma^2)}} \exp \left\{ -\frac{[\ln(1 + \delta)\sqrt{1 + \sigma^2}]^2}{2 \ln(1 + \sigma^2)} \right\} \frac{d\delta}{1 + \delta}. \quad (18)$$

Substituting (18) into (17), one finally obtains

$$P_{\ln}(\kappa) d\kappa = \frac{1}{\sqrt{2\pi \sigma_{\ln}^2}} \exp \left\{ -\frac{[\ln(1 + \kappa/|\kappa_{\min}|) + \sigma_{\ln}^2/2]^2}{2\sigma_{\ln}^2} \right\} \frac{d\kappa}{\kappa + |\kappa_{\min}|}, \quad (19)$$

where the quantity σ_{\ln} is defined by

$$\sigma_{\ln}^2 \equiv \ln \left(1 + \frac{\langle \kappa^2 \rangle}{|\kappa_{\min}|^2} \right). \quad (20)$$

Before discussing the application and validity of equation (19), two important remarks should be mentioned. First, recall that the lognormal distribution violates the assumption of hierarchical ansatz used in the derivation of equation (14). The resultant expression (19) is thus inconsistent, however, the violation of the hierarchical assumption is fortunately weak on nonlinear scales of interest here (e.g., Kayo et al. 2001). We therefore expect that, as long as we restrict ourselves to the range of applicability, the expression (19) can provide a reasonable approximation and capture an important aspect of the non-Gaussianity in the weak lensing field. Secondly, notice that the result (19) heavily relies on the validity of the approximation (16). One might suspect that the approximation breaks down for a case with the high source redshift such as $z_s \gtrsim 1$, where the lensing projection becomes more important, and this will be discussed below. Of course, one can directly evaluate the convergence PDF $P(\kappa)$ from equations (13) and (14) assuming the lognormal PDF of δ , although this treatment is not useful in practice. Instead, in this paper we *a priori* assume the simple analytic prediction (19), whereby we can further derive the useful analytic formulae for the Minkowski functionals and obtain a more physical interpretation of the results. We will then carefully check our model by comparing the predictions with the numerical simulation results.

3.2. Minkowski functionals

Expression (17) implies that the projection effect is primarily unimportant and is eliminated by rescaling the quantities $\delta \rightarrow \kappa/|\kappa_{\min}|$. That is, the statistical feature of κ directly reflects that of three-dimensional density δ . If this is the case, one can further develop a prediction of the weak lensing field based on the lognormal ansatz. To investigate this issue, the other informative statistics such as the higher-order correlation and the isodensity statistics should be examined.

Among these statistics, it is known that Minkowski functionals can be useful and give a morphological description to the contour map of the weak lensing field (e.g, Schmalzing & Buchert 1997). In a two-dimensional case, Minkowski functionals are characterized by the three statistical quantities: the area fraction, v_0 , circumference per unit length, v_1 and Euler characteristics per unit area, v_2 . The third functional is equivalent to the famous genus statistics often used in the cosmological context (Gott, Melott & Dickinson 1986). These quantities are evaluated for each isocontour as a function of level threshold, $\nu \equiv \kappa/\langle \kappa^2 \rangle$.

The explicit expression of Minkowski functional $v_0(\nu)$ is given by

$$v_0(\nu) = \langle \Theta(\kappa - \nu \langle \kappa^2 \rangle^{1/2}) \rangle, \quad (21)$$

where Θ denotes the Heaviside step function. The Minkowski functionals $v_1(\nu)$ and $v_2(\nu)$ provide an additional information on the convergence field, since the definitions include higher derivative terms such as $\partial_i \kappa$ and $\partial_i \partial_j \kappa$. According to Matsubara (2000), Minkowski functionals v_1 and v_2 in the two-dimension map can be related to the level-crossing and the genus statistics defined in the two-dimensional surface, N_1 and G_2 (see also Schmalzing & Buchert 1997):

$$v_1(\nu) = \frac{\pi}{8} N_1(\nu) = \frac{\pi}{8} \langle \delta_D(\kappa - \langle \kappa^2 \rangle^{1/2} \nu) |\partial_1 \kappa| \rangle, \quad (22)$$

$$v_2(\nu) = G_2(\nu) = \langle \delta_D(\kappa - \langle \kappa^2 \rangle^{1/2} \nu) \delta_D(\partial_1 \kappa) |\partial_2 \kappa| \partial_1 \partial_1 \kappa \rangle. \quad (23)$$

Assuming that the convergence field is approximately described by the lognormal distribution, the analytic expressions for Minkowski functionals can be derived in a straightforward manner. Since the area fraction represents the cumulative probability above the threshold ν , substituting (19) into the definition (21) yields

$$v_{0,\ln}(\nu) = \int_{\nu \langle \kappa^2 \rangle^{1/2}}^{+\infty} d\kappa P_{\ln}(\kappa) = \frac{1}{2} \operatorname{erfc} \left\{ \frac{y(\nu)}{\sqrt{2}} \right\} \quad (24)$$

with the function $y(\nu)$ given by

$$y(\nu) \equiv \frac{\sigma_{\ln}}{2} + \frac{\ln(1 + \nu \langle \kappa^2 \rangle^{1/2} / |\kappa_{\min}|)}{\sigma_{\ln}}. \quad (25)$$

As for the Minkowski functionals v_1 and v_2 , the analytic expressions for the lognormal distribution can be obtained from the local transformation of Gaussian formulae, $N_1(\nu)$ and $G_2(\nu)$. The details of the derivation are described by Taruya & Yamamoto (2001) (see also Matsubara & Yokoyama 1996). The final results become

$$v_{1,\ln}(\nu) = \frac{1}{8\sqrt{2}} \frac{1}{\sqrt{|\kappa_{\min}|^2 + \langle \kappa^2 \rangle}} \frac{\langle (\nabla \kappa)^2 \rangle^{1/2}}{\sigma_{\ln}} e^{-y^2(\nu)/2}, \quad (26)$$

$$v_{2,\ln}(\nu) = \frac{1}{2(2\pi)^{3/2}} \frac{1}{|\kappa_{\min}|^2 + \langle \kappa^2 \rangle} \frac{\langle (\nabla \kappa)^2 \rangle}{\sigma_{\ln}^2} y(\nu) e^{-y^2(\nu)/2}. \quad (27)$$

Note that in the limit $\langle \kappa^2 \rangle^{1/2} / |\kappa_{\min}| \ll 1$, the above predictions recover the Gaussian formulae:

$$v_{0,G}(\nu) = \frac{1}{2} \operatorname{erfc} \left(\frac{\nu}{2} \right), \quad (28)$$

$$v_{1,G}(\nu) = \frac{1}{8\sqrt{2}} \left(\frac{\langle (\nabla\kappa)^2 \rangle}{\langle \kappa^2 \rangle} \right)^{1/2} e^{-\nu^2/2}, \quad (29)$$

$$v_{2,G}(\nu) = \frac{1}{2(2\pi)^{3/2}} \frac{\langle (\nabla\kappa)^2 \rangle}{\langle \kappa^2 \rangle} \nu e^{-\nu^2/2}. \quad (30)$$

Apart from the PDF $P(\kappa)$ and the area fraction v_0 , there exists no clear reason that the extension of lognormal model to the Minkowski functionals v_1 and v_2 still provides a good approximation in the real universe. At present, the predictions (26) and (27) are just regarded as an *extrapolation* from the one-point PDF $P(\kappa)$ and should be checked by numerical simulations.

4. Comparison with ray-tracing simulations

In this section, we quantitatively examine the validity of lognormal model by comparing its predictions with the simulation results. A brief description of ray-tracing simulation is presented in section 4.1. In section 4.2, the model parameters in the lognormal formulae are checked in details using the simulation data. Some important numerical effects are also discussed. Then, section 4.3 describes our main results, i.e, the comparisons of one-point PDF and Minkowski functionals between the lognormal predictions and the simulation data.

4.1. Ray-tracing simulations

In order to investigate the lognormal property of convergence fields, we use a series of ray-tracing simulations in three cold dark matter models (SCDM, LCDM, OCDM for Standard, Lambda, Open CDM models, respectively). The cosmological parameters used here are summarized in Table 1.

To perform a ray-tracing simulation, a light-cone data set is first generated by particle-mesh (PM) N-body code. The PM code uses $256^2 \times 512$ particles and is performed in a periodic rectangular box of size $(L, L, 2L)$ with the force mesh $256^2 \times 512$. The initial conditions are generated according to the transfer functions of Bond & Efstathiou (1984). Then the light-cone of the particles is extracted from each simulation during the run (Hamana, Colombi & Suto 2001). The final set of light-cone data are created so as to cover a field of view of 5×5 square degrees and the box sizes of each output are chosen so as to match to the convergence of the light ray bundle. As a result, the angular resolution of ray-tracing simulation, which is basically limited by the spatial resolution of PM N-body code, becomes almost constant, $\theta_{\text{res}} \approx 1.5'$ from the observer at $z = 0$ (Hamana & Mellier 2001).

Once the light-cone data is obtained, ray-tracing simulations are next performed using the multiple lens-plane algorithm (e.g., Schneider, Ehlers & Falco 1992; Jain, Seljak & White 2000; Hamana, Martel & Futamase 2000). In our calculation, the interval between lens planes are fixed to comoving length, $80h^{-1}\text{Mpc}$. The 512^2 light rays are then traced backward from the observer’s point to the source plane. The initial ray directions are set on 512^2 grids and the two-dimensional deflection potential are calculated by solving ray-bundle equations keeping the same grids in each lens plane. We obtained 40 realizations by randomly shifting the simulation boxes.

After constructing the weak lensing map in the image plane at $z = 0$, the smoothed convergence field are finally computed on 512^2 grids by convolving the top-hat smoothing kernel. All the statistical quantities such as one-point PDF and Minkowski functionals are evaluated from the data. In a subsequent analysis, we use the convergence data set fixing the source redshifts to $z_s = 1$ and 2.

4.2. On the lognormal model parameters

Since the lognormal predictions presented in previous section heavily rely on the three parameters, κ_{\min} , $\langle\kappa^2\rangle$ and $\langle(\nabla\kappa)^2\rangle$, we first check them in some details using the ray-tracing simulations.

Figure 1 shows the minimum value of the convergence, κ_{\min} against the smoothing angle. The error-bars indicate the $1\text{-}\sigma$ errors around each mean, where the mean value κ_{\min} is obtained from 40 realization data. As stated in section 3.1, the convergence κ evaluated along an empty beam is theoretically considered as a possibility of κ_{\min} and expressed from equation (6) as

$$\kappa_{\text{empty}} = - \int_0^{\chi_s} d\chi w(\chi, \chi_s), \quad (31)$$

which implies that the light ray propagates through empty space with $\delta = -1$ everywhere along the line of sight. In figure 1, thick lines represent the theoretical prediction (31) for each model. Clearly, these predictions give much smaller values than the simulation results in both $z_s = 1.0$ and 2.0 cases. In addition to the systematic cosmological model dependences, the scale-dependence of κ_{\min} also appears.

These results mean that none of the light rays becomes completely empty beam (see also Jain, Seljak & White 1999). Nevertheless, one cannot exclude the possibility that some or even the majority of lines of sights become empty at scales smaller than the mean separation angle between particles of N-body simulations. In this sense, the minimum value κ_{\min} could be affected by the finite sampling from a limiting survey size of the convergence map. Based

on this consideration, we propose the following intuitive way to explain the behaviors of κ_{\min} shown in figure 1. Assuming that the original PDF of *infinitesimal* light rays obeys the lognormal model with the minimum value κ_{empty} , one can roughly estimate κ_{\min} from the condition that the expectation number of independent sampling area for $\kappa_{\text{empty}} \leq \kappa \leq \kappa_{\min}$ becomes unity in the field-of-view $5^\circ \times 5^\circ$. The details of estimation is described in Appendix A. For a given angular scale θ_{TH} and cosmological model, the quantity κ_{\min} is evaluated by solving the equation (A2) with the prior PDF (A1). The thin lines in figure 1 depict the estimation based on this prescription, which reasonably agrees with simulations. This result is interesting in the sense that we could analytically predict κ_{\min} and the resultant minimum value is sensitive to the cosmological parameters, especially Ω_0 . The practical possibility will be again discussed in the final section.

Next, turn to focus on the variances of the convergence and its gradient fields. In figure 2, the measured amplitudes, $\langle \kappa^2 \rangle^{1/2}$ and $\langle (\nabla \kappa)^2 \rangle^{1/2}$, are plotted in linear- and log-scale and are compared with linear (*short-dashed*) and nonlinear (*solid*) predictions. For the RMS of the convergence $\langle \kappa^2 \rangle^{1/2}$, the nonlinear prediction based on the Peacock & Dodds (1996) formula faithfully reproduces the simulation result over the smoothing angles, $\theta \gtrsim \theta_{\text{res}} \approx 1.5'$. On the other hand, in the case of $\langle (\nabla \kappa)^2 \rangle$, nonlinear predictions systematically deviate from simulations. The discrepancy remains even at larger smoothing angles, $\theta \sim 10'$ and causes $30 \sim 40\%$ error.

While the theoretical predictions based on the expressions (8) and (10) were computed assuming that the mass power spectrum $P_{\text{mass}}(k)$ are continuous and has infinite resolution, the simulation data is practically affected by the finite resolution. In our case, the limitation of PM force mesh could be attributed to the finite resolution or the cutoff of Fourier modes, which becomes influential even on larger smoothing angles, $\theta \gtrsim \theta_{\text{res}}$. In fact, compared to $\langle \kappa^2 \rangle$, dominant contribution to the quantity $\langle (\nabla \kappa)^2 \rangle$ comes from the short-wavelength modes of three-dimensional density fluctuations, sensitively depending on the choice of the smoothing filter. To show the significance of this effect, nonlinear prediction is modified according to the finite resolution of PM code (see Appendix B). Shortly, the Fourier-integrals in the expressions of (8) and (10) are discretized so as to mimic the PM N-body resolution as follows (Eqs.[B1][B2] in Appendix B):

$$\int_0^\infty dk_\perp \Delta^2(k_\perp) W_{\text{TH}}^2(k_\perp r \theta) \implies \sum_{n=1}^{N_{\text{max}}} \Delta k_\perp \Delta^2(k_{\perp,n}) W_{\text{TH}}^2(k_{\perp,n} r \theta),$$

$$\Delta^2(k_\perp) \equiv \begin{cases} (k_\perp/2\pi) P_{\text{mass}}(k_\perp) & \text{for } \langle \kappa^2 \rangle, \\ (k_\perp^3/2\pi) P_{\text{mass}}(k_\perp) & \text{for } \langle (\nabla \kappa)^2 \rangle. \end{cases},$$

where n -th Fourier mode $k_{\perp,n}$ is given by $k_{\perp,n} = \Delta k_\perp \times n$ and the interval Δk_\perp is set to

$$\Delta k_{\perp} = 2\pi/L_{\text{box}}(z).$$

The long-dashed lines in figure 2 show the results including the finite-resolution effect. In each panel, the number of Fourier modes, N_{max} is chosen as 90 (see discussion in Appendix B). It is apparent that the prediction of $\langle(\nabla\kappa)^2\rangle^{1/2}$ systematically reduces its power all over the scales and it almost reconciles with the simulation result, although the result of $\langle\kappa^2\rangle^{1/2}$ remains unchanged. We have also examined various cases by changing the maximum number to $64 \lesssim N_{\text{max}} \lesssim 128$, but obtained qualitatively similar behavior. Note that the incorrect prediction of $\langle(\nabla\kappa)^2\rangle$ leads to a systematic error in predicting the amplitude of the Minkowski functionals v_1 and v_2 from their definitions (26) and (27), while it does not alter the non-Gaussian shapes of those functionals with respect to the level threshold.

Keeping up the above remarks in mind, in what follows, to make a comparison with the lognormal models transparent, we use the parameters $\langle\kappa^2\rangle$, $\langle(\nabla\kappa)^2\rangle$ and κ_{min} directly estimated from the simulations when plotting the lognormal predictions (19), (24), (26) and (27).

4.3. Results

4.3.1. One-point PDF

As a quick view of the validity of lognormal model, we first deal with the one-point PDF, $P(\kappa)$. Figures 3 and 4 show the one-point PDFs of the local convergence in various CDM models with the smoothing angles, $\theta = 2'$, $4'$ and $8'$. Here, the PDF data is constructed by binning the data with $\Delta\kappa = 0.01$. The source redshifts are fixed to $z_s = 1.0$ in figure 3 and $z_s = 2.0$ in figure 4. Clearly, the functional form of the one-point PDF becomes broader as increasing the source redshift z_s . On small angular scales, the PDF significantly deviates from the Gaussian PDF denoted by dashed lines. Although local convergences on larger smoothing scales tend to approach the Gaussian form, they still exhibit a non-Gaussian tail.

In figures 3 and 4, solid lines represent the lognormal predictions (19), whose parameters κ_{min} and $\langle\kappa^2\rangle$ are directly estimated from simulations. The agreement between the lognormal model and the simulation results is generally good. In particular, at lower source redshift $z_s = 1.0$, the lognormal PDF accurately describes the non-Gaussian tails in the high-convergence region up to $\kappa \lesssim 10 \langle\kappa^2\rangle^{1/2}$. In the case of higher source redshift $z_s = 2.0$, the discrepancy becomes evident at larger smoothing scale. The lognormal PDF over-predicts in the high-convergence region, and under-predicts in the low-convergence region. This discrepancy might be ascribed to the projection effect of gravitational lensing (see eq.[6]), since the lognormal PDF is obtained based on the approximation (17), which cannot be validated

as increasing the source redshift z_s . Nevertheless, even in that case, a better agreement between lognormal model and simulations was found at small angular scales. These features are also seen in figure 5, where the differences between simulated PDF and lognormal PDF normalized by the simulated PDF, $[P_{\text{sim}}(\kappa) - P_{\text{ln}}(\kappa)]/P_{\text{sim}}(\kappa)$ are plotted as a function of level threshold $\nu = \kappa/\langle\kappa^2\rangle^{1/2}$, in the case of LCDM model.

Accurate lognormal-fit in the low- z_s case is amazing and is regarded as a considerable success. As a closer look at the non-Gaussian tails, however, lognormal PDF slightly underpredicts the simulations at low-density region, $\kappa < 0$ (see Fig.3 and upper-panel of Fig.5). Furthermore, at $\theta = 2'$, the simulation results generally tend to deviate from lognormal PDF in the highly non-Gaussian tails $\kappa \gtrsim 10 \langle\kappa^2\rangle^{1/2}$, although the prediction still remains consistent within the $1\text{-}\sigma$ error. In particular, in the case of the OCDM model, the discrepancy becomes apparent even at $\kappa \gtrsim 8 \langle\kappa^2\rangle^{1/2}$. The systematic deviation seen in non-Gaussian tails might be ascribed to the presence of virialized objects. Notice that the angular scale $\theta = 2'$ corresponds to the effective smoothing scale $R \sim 0.5h^{-1}\text{Mpc}$ at mean redshift $z \sim 0.5$. This indicates that high- κ value is attained by the light-ray propagating through the high-density region in the very massive halos with $M \gtrsim 10^{14}h^{-1}M_\odot$. Indeed, highly non-Gaussian tails of convergence PDF sensitively depends on the detailed structure of non-linear objects, as pointed out by Kruse & Schneider (2000). They construct an analytic model of one-point PDF based on the universal profile of dark matter halos and the Press-Schechter theory for halo abundance. Since the virialized halos induce the highly non-Gaussian tails of the local convergence, their treatment would be helpful to describe the non-Gaussian tails of PDF. In contrast, due to the lack of physical bases, no reliable prediction is expected from the empirical lognormal model.

Another reason for discrepancy might be the choice of the parameter, κ_{min} . Strictly speaking, minimum value of κ seen in the simulated PDF represents a rare event for the whole data sets, which are not rigorously equivalent to the averaged value of 40 realization data shown in figure 1. We have also examined the lognormal-fit adopting the minimum value of the PDF data for κ_{min} . The thin-lines in figure 5 show the results in LCDM case adopting the actual minimum value κ of each PDF data. The results seem somehow improved at small angle $\theta = 2' \sim 4'$ in high- z_s cases, but we rather recognize the fact that lognormal-fit to the high-density region is sensitive to the choice of κ_{min} .

Except for these details, lognormal model of one-point PDF remains a fairly accurate model of the convergence field, at least, up to $\kappa \sim 5\langle\kappa^2\rangle^{1/2}$ and is indeed applicable even at small angular scales such as $2' \lesssim \theta \lesssim 4'$, irrespective of the assumption, (16) or (17).

4.3.2. Minkowski functionals

Having recognized the successful lognormal-fit to the one-point PDF, we next investigate the lognormal model of Minkowski functionals. For this purpose, we restrict our analysis to the source redshift $z_s = 1.0$. Here, the Minkowski functionals for a simulated convergence map are calculated by the method developed by Winitzki & Kosowsky (1997).

Figure 6 shows the results in various CDM models fixing the smoothing angle $\theta = 2.0'$. The Minkowski functionals are plotted against the level threshold $\nu = \kappa/\langle\kappa^2\rangle^{1/2}$ with the interval, $\Delta\nu = 0.5$, so that data in each bin is approximately regarded as statistically independent. The solid lines depict the lognormal predictions (24), (26) and (27).

Similar to the one-point PDF, a significant non-Gaussian signature is detected from the asymmetric shape of the Minkowski functionals, especially from the Euler characteristic v_2 . In marked contrast with the Gaussian predictions, the lognormal predictions remarkably reproduce the simulation results, not only the shape dependences but also the amplitudes. The agreement between lognormal prediction and simulations still remains accurate over the rather wider range, $-4 < \nu < 4$, where the discrepancy seen in the one-point PDF of the OCDM model is not observed. Since the prediction has no adjustable parameter and only uses the information from an output data, this agreement is successful.

Figure 7 depicts the results with various smoothing angles fixing the cosmology to LCDM model. For illustrative purpose, the amplitudes of v_1 and v_2 at the smoothing angle $\theta = 4'$ and $8'$ are artificially changed by multiplying the factors as indicated in each panel, in order to make the non-Gaussianity manifest. The Minkowski functionals tend to approach the Gaussian prediction as increasing the smoothing angle, consistent with the behaviors of one-point PDF. The results in other cosmological models are also similar and the agreement between lognormal models and simulations is satisfactory.

To manifest the accuracy of the lognormal-fit in contrast to the other existing analytical models, let us now consider the perturbation predictions. Employing the Edgeworth expansion, the perturbative expressions for Minkowski functional are derived analytically (Matsubara 2000; Sato et al. 2001):

$$v_0(\nu) \simeq v_{0,G}(\nu) + \langle\kappa^2\rangle^{1/2} \frac{1}{6\sqrt{2\pi}} e^{-\nu^2/2} S_3^{(0)} H_2(\nu), \quad (32)$$

$$v_1(\nu) \simeq v_{1,G}(\nu) \left[1 + \langle\kappa^2\rangle^{1/2} \left\{ \frac{S_3^{(0)}}{6} H_3(\nu) + \frac{S_3^{(1)}}{3} H_1(\nu) \right\} \right], \quad (33)$$

$$v_2(\nu) \simeq v_{2,G}(\nu) \left[1 + \frac{\langle\kappa^2\rangle^{1/2}}{H_0(\nu)} \left\{ \frac{S_3^{(0)}}{6} H_4(\nu) + \frac{2S_3^{(1)}}{3} H_2(\nu) + \frac{S_3^{(2)}}{3} \right\} \right]. \quad (34)$$

Notice that in the case of the three-dimensional density field, the above expansion is valid up to the RMS of δ , $\sigma \lesssim 0.3$ (Matsubara & Yokoyama 1996; Matsubara & Suto 1996), which can be translated into the condition, $\langle \kappa^2 \rangle^{1/2} \lesssim 0.3 |\kappa_{\min}|$. Here, the function $H_n(\nu)$ denotes n -th order Hermite polynomial, $H_n(x) \equiv (-1)^n e^{x^2/2} (d/dx)^n e^{-x^2/2}$, and the quantities $S_3^{(i)}$ represent the skewness parameters defined as

$$S_3^{(0)} = \frac{\langle \kappa^3 \rangle}{\langle \kappa^2 \rangle^2}, \quad (35)$$

$$S_3^{(1)} = -\frac{3}{4} \frac{\langle \kappa^2 \cdot \nabla^2 \kappa \rangle}{\langle \kappa^2 \rangle \langle (\nabla \kappa)^2 \rangle}, \quad (36)$$

$$S_3^{(2)} = -3 \frac{\langle (\nabla \kappa \cdot \nabla \kappa) \nabla^2 \kappa \rangle}{\langle (\nabla \kappa)^2 \rangle^2}. \quad (37)$$

Equations (32)-(34) imply that, in the weakly nonlinear regime, the non-Gaussian features on the Minkowski functionals can be completely described by the above parameters, which can be evaluated by the second-order perturbation theory of structure formation (e.g., Bernardeau et al. 1997). It is worth noting that in the case of the lognormal model, all the skewness parameters, $S_3^{(\alpha)}$ are equal to 3 (Hikage, Taruya & Suto 2001).

Figure 8 plots the perturbation results in LCDM model. The source redshift is fixed to $z_s = 1.0$. The solid lines represent the results in which the skewness parameters are evaluated using the second-order perturbation theory (*perturb 1*), while the dashed lines depict the results using those estimated from simulations (*perturb 2*). In both cases, the variances $\langle \kappa^2 \rangle$ and $\langle (\nabla \kappa)^2 \rangle$ in the expressions (32)-(34) are estimated from simulations. Also, in figure 9, the comparison between various model predictions is summarized, introducing the fractional error, defined by

$$\text{Err}[v_i(\nu)] \equiv \frac{v_i^{(\text{sim})}(\nu) - v_i^{(\text{model})}(\nu)}{v_{i,\text{max}}^{(\text{sim})}}, \quad (38)$$

with the quantity $v_{i,\text{max}}^{(\text{sim})}$ being the maximum value of $v_i(\nu)$ among the mean values of the simulation for each Minkowski functional: $v_{0,\text{max}}^{(\text{sim})} = 1.0$, $v_{1,\text{max}}^{(\text{sim})} = 0.040$ and $v_{2,\text{max}}^{(\text{sim})} = 0.0042$ at angular scale $\theta = 2'$, for instance. As a reference, the $1\text{-}\sigma$ error of simulation results is plotted as error-bars around zero mean in each panel.

At the large smoothing angle $\theta = 8'$, both of the perturbation results tend to reconcile with each other and fit to the simulation results well within the $1\text{-}\sigma$ error. As the smoothing angle decreases, however, the perturbation results cease to fit the simulations, because the RMS of local convergence reach $\langle \kappa^2 \rangle^{1/2} \gtrsim 0.4 |\kappa_{\min}|$ and the Edgeworth expansion breaks down. Furthermore, the second-order perturbations under-predict the skewness parameters, compared with those estimated from simulations, which lead to the different predictions (compare *perturb 1* with *perturb 2* in left- and middle-panels in Figs.8, 9). In particular,

the circumference v_1 shows a peculiar behavior, $v_1 < 0$, which is not allowed by definition. Notice that even in these cases, the fractional error $\text{Err}[v_i(\nu)]$ in the lognormal prediction still remains smaller, although the systematic deviations in every model are not so large.

From these discussions, we conclude that the empirical lognormal models can provide a good approximation for the Minkowski functionals, compared to the current existing models.

5. Consistency with higher-order moments

Since the skewness of the local convergence has been proposed as a simple statistical estimator of non-Gaussian signature to determine the cosmological parameters, various authors have investigated the usefulness of this quantity using ray-tracing simulations. These analyses have revealed that the skewness at small-angle $\theta \lesssim 10'$ exhibits the significant influence of nonlinear clustering and a more reliable theoretical model beyond the perturbation theory is needed. According to these facts, non-perturbative predictions based on the “hyper-extended perturbation theory” (Scoccimarro & Frieman 1999) or non-linear fitting formula of bi-spectrum (Scoccimarro & Couchman 2001) are examined (Hui, 1998; Van Waerbeke et al. 2001b).

In general, the one-point PDF as well as the Minkowski functionals characterizes a family of higher-order statistics. Hence, as a consistency check of the lognormal prediction, it seems natural to analyze the higher-order moments of local convergence. From an empirical lognormal PDF (19), the skewness and the kurtosis of the local convergence defined by $S_{3,\kappa} \equiv \langle \kappa^3 \rangle / \langle \kappa^2 \rangle^2$ and $S_{4,\kappa} \equiv (\langle \kappa^4 \rangle - 3\langle \kappa^2 \rangle^2) / \langle \kappa^2 \rangle^3$ are respectively given by

$$S_{3,\kappa} = \frac{1}{|\kappa_{\min}|} \left(3 + \frac{\langle \kappa^2 \rangle}{|\kappa_{\min}|^2} \right), \quad (39)$$

$$S_{4,\kappa} = \frac{1}{|\kappa_{\min}|^2} \left\{ 16 + 15 \frac{\langle \kappa^2 \rangle}{|\kappa_{\min}|^2} + 6 \left(\frac{\langle \kappa^2 \rangle}{|\kappa_{\min}|^2} \right)^2 + \left(\frac{\langle \kappa^2 \rangle}{|\kappa_{\min}|^2} \right)^3 \right\}. \quad (40)$$

Figure 10 shows the direct measurement of $S_{3,\kappa}$ and $S_{4,\kappa}$ fixing the source redshift to $z_s = 1.0$. The error-bars indicates 1- σ error estimated from the 40 realization data. The lognormal predictions (39) and (40) are depicted as solid lines.

In practice, the convergence field κ in numerical simulation does not extend the entire range between κ_{\min} and $+\infty$, but is limited as $\kappa_{\min} < \kappa < \kappa_{\max}$, due to the finite sampling effect from a limited size of simulation data (see Kayo et al. 2001 in the case of three-

dimensional density field δ). Thus, the n -th order moments of κ given by

$$\langle \kappa^n \rangle = \int_{\kappa_{\min}}^{\kappa_{\max}} d\kappa P_{\ln}(\kappa) \kappa^n \quad (41)$$

may provide a better description in evaluating the skewness $S_{3,\kappa}$ and the kurtosis $S_{4,\kappa}$.

The dashed lines in figure 10 show the lognormal prediction based on the equation (41), where the cutoff parameter κ_{\max} is adopted as the averaged maximum value from each realization data. In contrast to the accurate fit seen in the one-point PDF, the lognormal-fit of skewness and kurtosis seems very poor. The prediction without cutoff κ_{\max} tends to over-predict as increasing smoothing angle, which shows opposite behavior compared to the simulations. As for the lognormal model based on (41), while the predictions reduce their amplitudes and broadly agree with simulations in the case of $S_{4,\kappa}$, they still exhibit some systematic discrepancies in $S_{3,\kappa}$. We have also examined the lognormal-fit adopting the minimum and maximum values of PDF data itself, but the result is not improved drastically.

At first glance, these discrepancies seem to contradict with the results in one-point PDF, however, a closer look at one-point PDF reveals that the lognormal PDFs slightly under-predict the simulation results at the low-density region. This tiny discrepancy may be ascribed to the overestimation of skewness. In other words, the skewness as well as kurtosis is very sensitive to the rare events, i.e, high- and low-convergence parts of the non-Gaussian tails. This sensitivity is clearly shown in the OCDM model. The simulated PDF at smoothing angle $\theta = 2'$ exhibits a highly non-Gaussian tails and it overshoots the lognormal prediction (see upper-right panel in Fig.3). The resultant skewness and kurtosis yield values larger than those of lognormal prediction. On the other hand, in SCDM and LCDM models, lognormal PDFs accurately fit to the highly non-Gaussian tails and thereby the predictions of skewness and kurtosis becomes relatively consistent with simulations, at least on the small scales, $2' \leq \theta \leq 4'$.

Therefore, the lognormal model of convergence does not provide an accurate prediction for the statistics sensitive to the rare events. This disagreement simply reflects the fact that the empirical lognormal model does not correctly describe projected structure of dark matter halos. On the other hand, a sophisticated non-perturbative model based on the hyper-extended perturbation theory or fitting formula of bi-spectrum is constructed so as to reproduce the N-body results of higher-order moments, which can provide an accurate prediction for the convergence skewness (Hui, 1998; Van Waerbeke et al. 2001b). Hence, for the prediction of higher-order moments, the non-perturbative model is more useful and reliable than the lognormal model. In contrast, the lognormal model fairly describes non-Gaussianity around the peak of the PDFs over the broad range, $\kappa \lesssim 5 \langle \kappa^2 \rangle^{1/2}$, which cannot be described by such a non-perturbative model. Thus, at least as a complementary approach, the log-

normal model is useful beyond the perturbative theory, and applicable in characterizing the one-point PDF and the Minkowski functionals.

6. Conclusion and Discussion

In the present paper, we have quantitatively investigated the extent to which the lognormal model fairly describes the statistics of weak lensing fields on linear and nonlinear scales using the ray-tracing simulations. The validity of lognormal model has been checked in details by comparing the lognormal predictions of the one-point PDF and the Minkowski functionals of convergence field with their simulation results.

The convergence field seen in the one-point PDF and the Minkowski functionals displays the non-Gaussian feature and significantly deviates from the Gaussian predictions. We have shown that the analytic formulae for lognormal models are useful and accurately describe the simulation results on both small and large smoothing angular scales in the case of the low- z_s data, while the perturbative prediction by Edgeworth expansion fails to reproduce the simulation results on small scales because of the nonlinearity of the underlying three-dimensional density field. The detailed comparison revealed that the lognormal model does not provide an accurate prediction for the statistics sensitive to the rare events such as the skewness and kurtosis of the convergence. We therefore conclude that, as long as we are concerned with the appropriate range of the convergence, $\kappa \lesssim 5 \langle \kappa^2 \rangle^{1/2}$, the lognormal model empirically but quantitatively gives a useful approximation characterizing the non-Gaussianity features on the convergence field.

The results obtained here will lead to an important improvement for the estimation of cosmological parameters using the Minkowski functionals (Sato, Takada, Jing & Futamase 2001). Although the original methodology has been proposed with the use of the Edgeworth formulae, (32)-(34), a more reliable estimation of cosmological parameters will be possible using the lognormal models. In the light of this, a reliable theoretical prediction for the model parameters of the lognormal formulae κ_{\min} , $\langle \kappa^2 \rangle$ and $\langle (\nabla \kappa)^2 \rangle$ should be further explored. As shown in figures 1 and 2, the simulation results reveal that κ_{\min} is very sensitive to the density parameter Ω_0 , while the $\langle \kappa^2 \rangle$ and $\langle (\nabla \kappa)^2 \rangle$ depend on Ω_0 and σ_8 . Such predictions will offer a new opportunity to determine the cosmological parameters, independently of the method using the higher-order moment, $S_{3,\kappa}$. In particular, if we do not focus on the overall normalization of the Minkowski functionals v_1 and v_2 controlled by the $\langle \kappa^2 \rangle$ and $\langle (\nabla \kappa)^2 \rangle$, the non-Gaussian features on those functionals are primarily controlled by κ_{\min} , and, for example, the intuitive way to predict κ_{\min} discussed in Appendix A could be used in constraining Ω_0 . Of course, for proper comparison with observation, there are other systematic effects we have

to take into account. One is the redshift distribution of source galaxies. Another important effect is the contamination by the intrinsic source ellipticity. This not only reduces the signal-to-noise ratio, but also systematically affects the non-Gaussianity of the weak lensing signal (Jain, Seljak & White 2000). These effects should be correctly incorporated into the lognormal predictions. These issues are now in progress, and will be presented elsewhere.

The statistics of cosmic shear directly reflect the statistical feature of mass distribution and using this fact, one might even discriminate the nature of dark matter. Furthermore, the weak lensing statistics have a potential to reveal the nonlinear and stochastic properties of galaxy biasing. In any cases, we expect that the lognormal property of the weak lensing field is helpful and plays an important role in extracting the various cosmological information.

We thank J.Sato for providing us the code to calculate the Minkowski functionals from the ray tracing simulation data. We also thank Y.Suto for careful reading of the manuscript and critical comments, C.Hikage for invaluable discussion, T.Buchert and M.Bartelmann for useful comments. I.K is supported by Takenaka-Ikueikai Fellowship. T.H. and M.T acknowledge supports from Japan Society for Promotion of Science (JSPS) Research Fellowships.

A. Influence of finite sampling on estimation of κ_{\min}

Minimum value of the convergence, κ_{\min} is theoretically expected to be equal to κ_{empty} (eq.[31]). In practice, however, the minimum value estimated from the simulation data can be systematically larger than those obtained from the empty beam, due to the finite sampling from the limiting survey area.

To see the influence of the finite sampling effect, let us roughly estimate the minimum value, κ_{\min} . Assuming that the *prior* one-point PDF, $P^{(\text{prior})}(\kappa)$ is approximately described by the lognormal PDF, in which the minimum value is characterized by κ_{empty} instead of the actual value κ_{\min} :

$$P^{(\text{prior})}(\kappa) = \frac{1}{\sqrt{2\pi}\sigma_{\ln}} \exp \left\{ -\frac{[\ln(1 + \kappa/|\kappa_{\text{empty}}|) + \sigma_{\ln}^2/2]^2}{2\sigma_{\ln}^2} \right\} \frac{d\kappa}{\kappa + |\kappa_{\text{empty}}|}, \quad (\text{A1})$$

with the quantity σ_{\ln}^2 being $\ln(1 + \langle \kappa^2 \rangle / |\kappa_{\text{empty}}|^2)$. Then the probability that the observed minimum value κ_{\min} systematically deviates from κ_{empty} is given by

$$\int_{-|\kappa_{\text{empty}}|}^{-|\kappa_{\min}|} d\kappa P^{(\text{prior})}(\kappa) = \frac{\pi\theta_{\text{TH}}^2}{\theta_{\text{field}}^2}, \quad (\text{A2})$$

where θ_{TH} is the top-hat smoothing angle, θ_{field} is field-of-view angle. The right hand side of equation (A2) represents the lower limit of probability determined from the expectation number of independent sampling area. The minimum value κ_{\min} is obtained by solving equation (A2).

Based on the equation (A2), the resultant values of κ_{\min} are summarized in figure 1 (*thin-lines*). Here, the field-of-view angle θ_{field} is fixed to 5° and the parameters in the prior lognormal PDF, $\langle \kappa^2 \rangle$ and κ_{empty} are computed according to the theoretical predictions (8) and (31), respectively.

B. Effect of finite resolution and variances $\langle \kappa^2 \rangle$ and $\langle (\nabla\kappa)^2 \rangle$

Statistical analysis based on the N-body simulation with PM algorithm should be carefully treated if we deal with the statistics on small scales. In our ray-tracing simulation, the box size of each simulation, $L_{\text{box}}(z)$, are determined so as to satisfy the resolution angle $\theta_{\text{res}} \approx 1.5'$, i.e, $L_{\text{box}}(z) \approx r(\chi(z))\theta_{\text{res}}$. The mesh of the PM algorithm is fixed to $252^2 \times 512$ in each simulation box. Among these parameters, the number of mesh severely restricts the Fourier modes of mass fluctuations, which could affect the evaluation of $\langle \kappa^2 \rangle$ and $\langle (\nabla\kappa)^2 \rangle$, depending on the choice of smoothing filter.

In order to investigate the significance of finite mesh-size, the theoretical predictions (8) and (10) are modified according to the PM N-body code. Since the influence of finite mesh-size mainly affects the high-frequency part of the fluctuations, the Fourier-integrals in the expressions (8) and (10) are modified to

$$\int_0^\infty dk_\perp \Delta^2(k_\perp) W_{\text{TH}}^2(k_\perp r\theta) \implies \sum_{n=1}^{N_{\text{max}}} \Delta k_\perp \Delta^2(k_{\perp,n}) W_{\text{TH}}^2(k_{\perp,n} r\theta), \quad (\text{B1})$$

where

$$\Delta^2(k_\perp) \equiv \begin{cases} (k_\perp/2\pi) P_{\text{mass}}(k_\perp) & \text{for } \langle \kappa^2 \rangle, \\ (k_\perp^3/2\pi) P_{\text{mass}}(k_\perp) & \text{for } \langle (\nabla\kappa)^2 \rangle. \end{cases} \quad (\text{B2})$$

The n -th Fourier mode $k_{\perp,n}$ is given by $k_{\perp,n} = \Delta k_\perp \times n$ and the interval Δk_\perp is set to $\Delta k_\perp = 2\pi/L_{\text{box}}(z)$.

In the above modification, the number of Fourier modes, N_{max} might be crucial in evaluating the quantity sensitive to the high frequency mode, which is related to the number of mesh, $N_{\text{mesh}} = 256$. Recall that the Nyquist frequency restricts the high-frequency mode to $k_{\text{Nyq}} = (\Delta k_\perp/2)N_{\text{mesh}}$, which implies $N_{\text{max}} = N_{\text{mesh}}/2$. Further, the number of independent Fourier mode is reduced by the factor 1/2 in evaluating the power spectrum. Thus, the high-frequency cutoff is roughly given by $k_{\text{cut}} \approx \sqrt{2} \times \Delta k_\perp (N_{\text{mesh}}/4)$, which yields

$$N_{\text{max}} = \frac{N_{\text{mesh}}}{2\sqrt{2}} \approx 90. \quad (\text{B3})$$

The long-dashed lines in figure 2 represent the results taking into account the finite mesh-size. Here, the nonlinear mass power spectrum $P_{\text{mass}}(k)$ by Peacock & Dodds (1996) is used in evaluating the discretized Fourier-integral (B1). We also examined the various cases by changing the maximum number, $64 < N_{\text{max}} < 128$, but obtained qualitatively similar behavior: the prediction $\langle (\nabla\kappa)^2 \rangle$ systematically reduces its power all over the scales, while the amplitude of $\langle \kappa^2 \rangle$ almost remains unchanged. Further, similar modification to the z -integral has been made so as to match the number of multiple lens-plane, however, this does not affect the final results.

REFERENCES

- Bacon, D., Refregier, A., & Ellis, R. 2000, MNRAS, 318, 625
- Bartelmann, M., & Schneider, P. 2001, Phys. Rep. 340, 291
- Bernardeau, F., Van Waerbeke, L., & Mellier, Y. 1997, A&A, 322, 1
- Blandford, R. D., Saust, A. B., Brainerd, T. G., & Villumsen, J. V. 1991, MNRAS, 251, 600
- Bouchet, F., Strauss, M.A., Davis, M., Fisher, K.B., Yahil, A., & Huchra, J.P. 1993, ApJ, 417, 36
- Bi, H.G., & Davidsen, A.F. 1997, ApJ, 479, 523
- Bond, J.R., & Efstathiou, G. 1984, ApJ, 285, L45
- Coles, P., & Jones, B. 1991, MNRAS, 248, 1
- Gott, J. R., Melott, A. L, & Dickinson, M., 1986, ApJ, 306, 341
- Hamana, T., & Mellier, Y. 2001, MNRAS, 327, 169
- Hamana, T., Colombi, S., & Suto, Y. 2001, A&A , 367, 18
- Hamana, T., Martel, H. & Futamase, T. 2000, ApJ, 529, 56
- Hamilton, A.J.S. 1985, ApJ, 292, L35
- Hikage, C., Taruya, A., & Suto, Y. 2001, ApJ, 556, 641
- Hu, W. 2001, Phys. Rev. D., 62, 043007
- Hui, L. 1999, ApJ, 519, L9
- Jain, B., & Seljak, U. 1997, ApJ, 484, 560
- Jain, B., Seljak, U., & White, S.D.M. 2000, ApJ, 530, 547
- Kaiser, N. 1992, ApJ, 388, 272
- Kaiser, N., & Squires, G, 1993, ApJ, 404, 441
- Kaiser, N., Wilson, G., & Luppino, G.A. 2000, preprint(astro-ph/0003338)
- Kayo, I., Taruya, A., & Suto, Y. 2001, ApJ, 561, 22

- Kofman, L., Bertschinger, E., Gelb, J.M., Nusser, A., & Dekel, A. 1994, ApJ, 420, 44
- Kruse, G., & Schneider, P. 2000, MNRAS, 318, 321
- Maoli, R., Van Waerbeke, L., Mellier, Y., Schneider, P., Jain, B., Bernardeau, F., Erbe, T., & Fort, B. 2001, A&A 368, 766
- Matsubara, T., & Suto, Y. 1996, ApJ, 460, 51
- Matsubara, T., & Yokoyama, J. 1996, 463, 409
- Matsubara, T. 2000, ApJ, submitted (astro-ph/0006269).
- Matsubara, T., & Jain, B. 2001, ApJ, 552, L89
- Mellier, Y. 1999, ARAA, 37, 127
- Metcalf, R. B., & Silk, J. 1999, ApJ, 519, L1
- Miralda-Escude, J. 1991, ApJ, 380, 1
- Mo, H.J., & White, S.D.M. 1996, MNRAS, 282, 347
- Munshi, B., & Jain, B. 2000, MNRAS, 318, 109
- Peacock, J.A., & Dodds, S.J. 1996, MNRAS, 280, L19
- Rhodes, J., Refregier, A., & Groth, E. 2001, ApJ, 552, L85
- Sato, J., Takada, M., Jing, Y.P., & Futamase, T. 2001, ApJ, 551, L5
- Schmalzing, J., & Buchert, T. 1997, ApJ, 482, L1
- Schneider, P., Ehlers, J., & Falco, C.C. 1992, *Gravitational Lenses* (Springer-Verlag, New York)
- Scoccimarro, R., & Couchman, H. 2001, MNRAS, 325, 1312
- Scoccimarro, R., & Frieman, J. 1999, ApJ, 520, 35
- Seljak, U., & Holtz, D. E. 1999, A&A, 351, L10
- Taruya, A., & Suto, Y. 2000, ApJ, 542, 559
- Taruya, A., & Yamamoto, K. 2001, ApJ, 550, 528
- Valageas, P. 2000, A & A, 356, 771

Van Waerbeke, L. et al. 2000, *A&A*, 358, 30

Van Waerbeke, L. et al. 2001a, *A&A*, 374, 757

Van Waerbeke, L., Hamana, T., Scoccimarro, R., Colombi, S., & Bernardeau, F., 2001b, *MNRAS*, 322, 918

Winitzki, S., & Kosowsky, A. 1997, *NewA*, 3, 75

Wittman, D.M., Tyson, J.A., Kirkman, D., Dell’Antonio, I., & Bernstein, G. 2000, *Nature*, 405, 143

Table 1. Cosmological parameters used in N-body simulations.

Model	Ω_0	λ_0	h	σ_8
SCDM	1.0	0.0	0.5	0.6
LCDM	0.3	0.7	0.7	0.9
OCDM	0.3	0.0	0.7	0.85

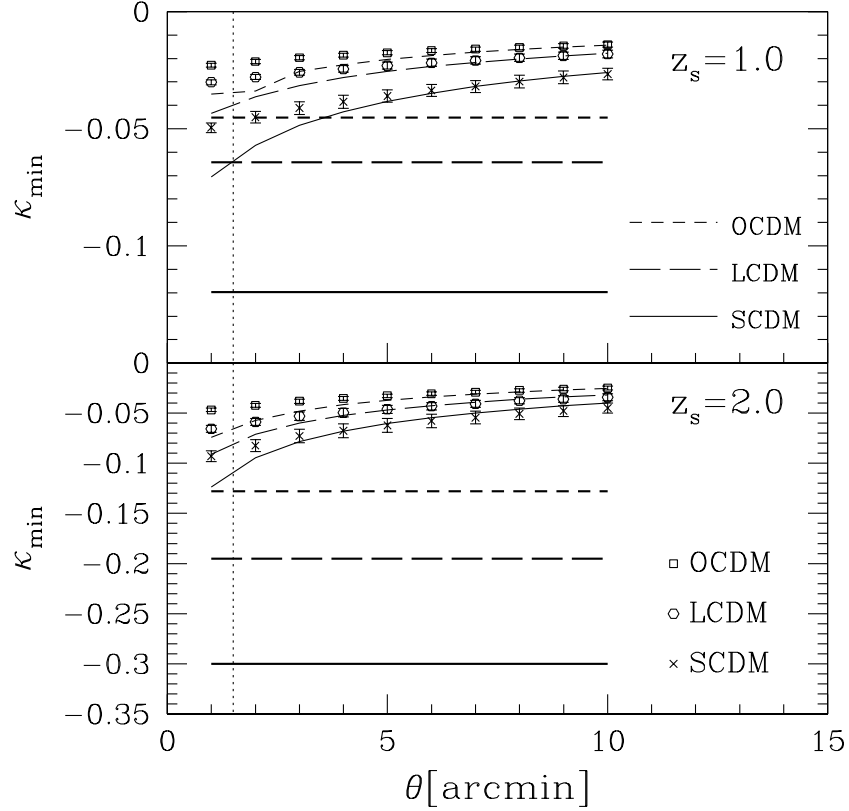


Fig. 1.— Minimum values of the convergence field, κ_{\min} , evaluated from the simulations. Thick lines indicate the predictions assuming the empty beam (see eq.[31]). The thin lines represent the estimation taking account of the effect of finite sampling (see Appendix A). The vertical dotted lines denote the resolution limit of ray-tracing simulation, which is primarily determined by the force resolution of PM N-body code (see text in Sec.4.1): $z_s = 1.0$ (*upper panel*); $z_s = 2.0$ (*lower panel*).

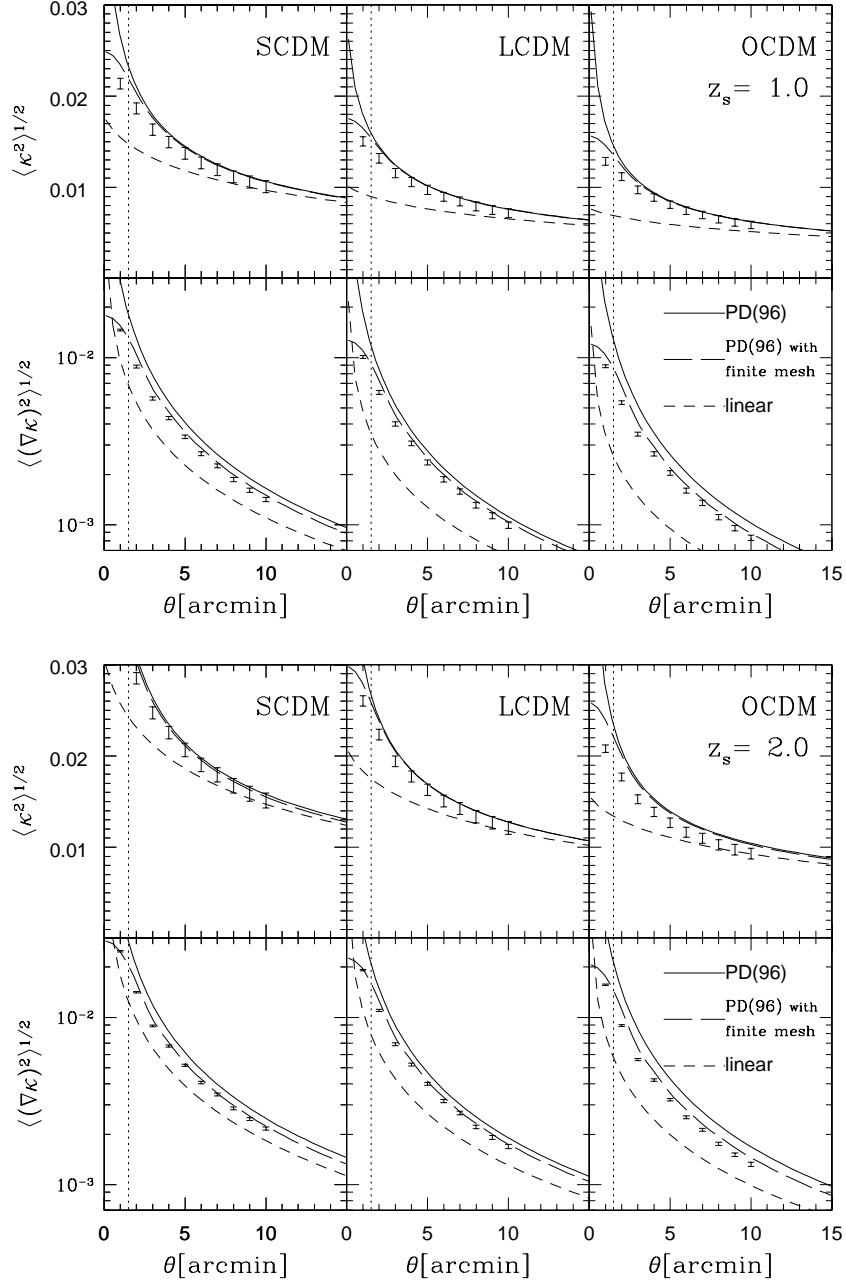


Fig. 2.— RMS of convergence field(*upper-panel*) and its gradient field (*lower-panel*) as a function of smoothing angle, plotted in linear- and log-scales. The error-bars indicate the simulation results, where error-bars are estimated from the 40 realization of ray-tracing data by randomly shifting each simulation boxes. The solid and short-dashed lines represent the theoretical prediction based on the expressions (8) and (10). In evaluating these equations, nonlinear mass power spectra by Peacock & Dodds (1996) are adopted in solid lines, while the linear power spectra are used in short-dashed lines. The long-dashed lines also represent the nonlinear prediction, but taking account of the finite resolution of PM N-body simulations (see Appendix B for details): SCDM model (*Left*) ; LCDM model (*Middle*) ; OCDM model (*Right*) of $z_s = 1.0$ cases(*Upper-panel*) and $z_s = 2.0$ cases(*Lower-panel*).

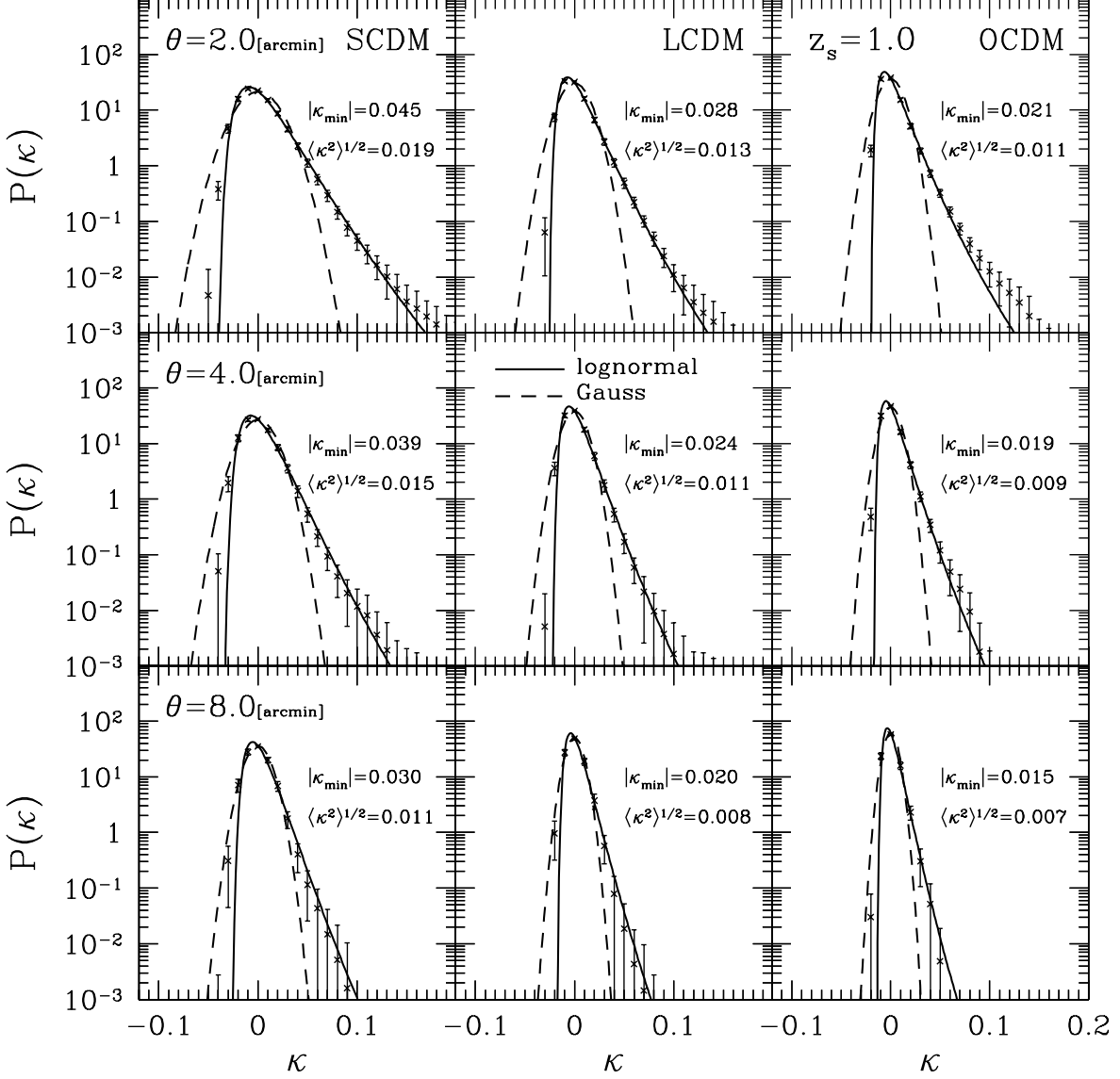


Fig. 3.— One-point PDFs of the convergence field fixing the source redshift to $z_s = 1.0$ with smoothing angle $\theta = 2'$, $4'$ and $8'$ (top to bottom). Solid lines show the lognormal prediction (eq.[19]), where the parameters κ and $\langle \kappa^2 \rangle$ are directly estimated from simulations. For comparison, the Gaussian PDF with the same variance $\langle \kappa^2 \rangle$ are plotted as dashed lines: SCDM model (left) ; LCDM model (middle) ; OCDM model (right).

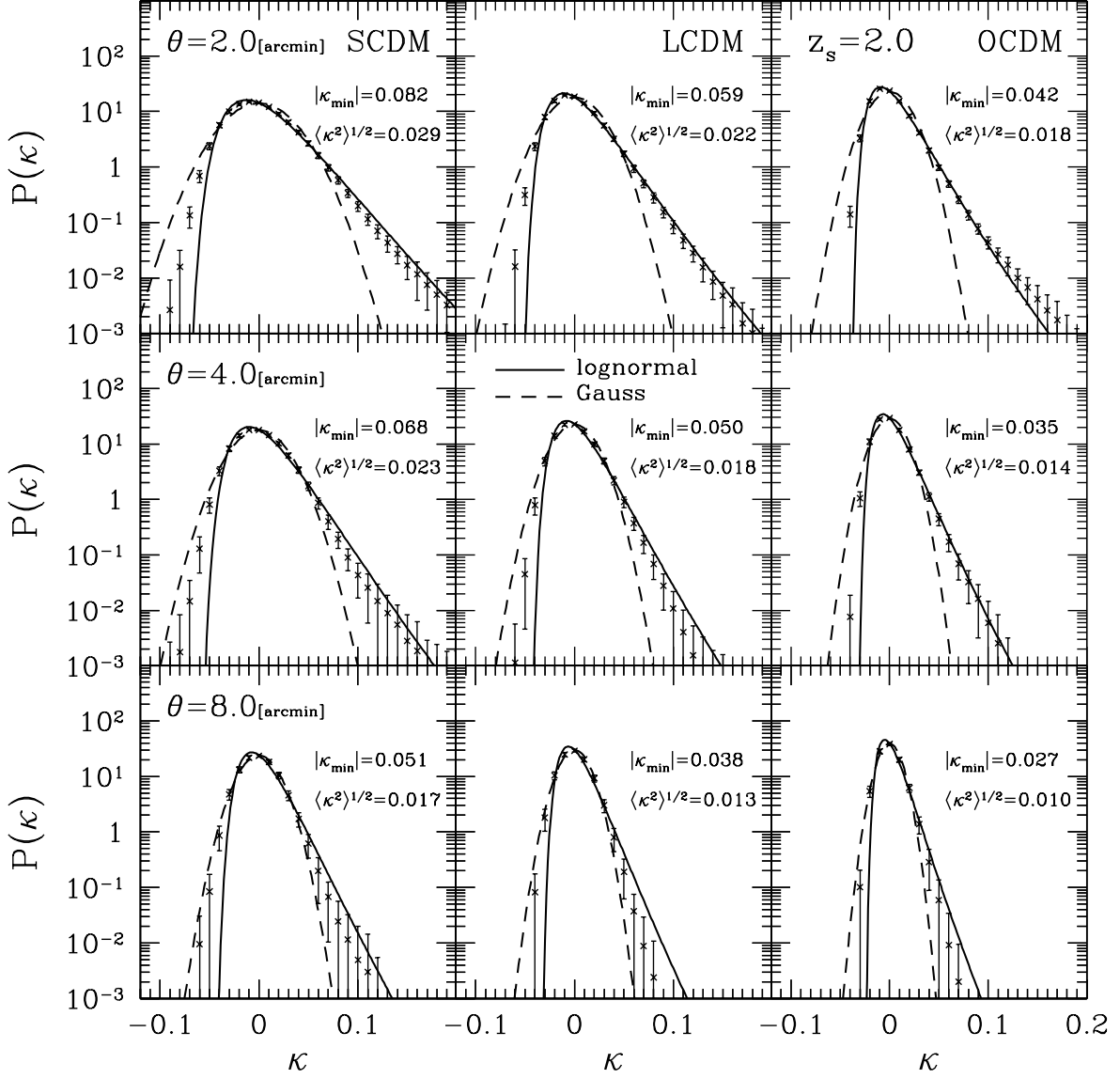


Fig. 4.— Same as Figure 3, but we fix the source redshift $z_s = 2.0$.

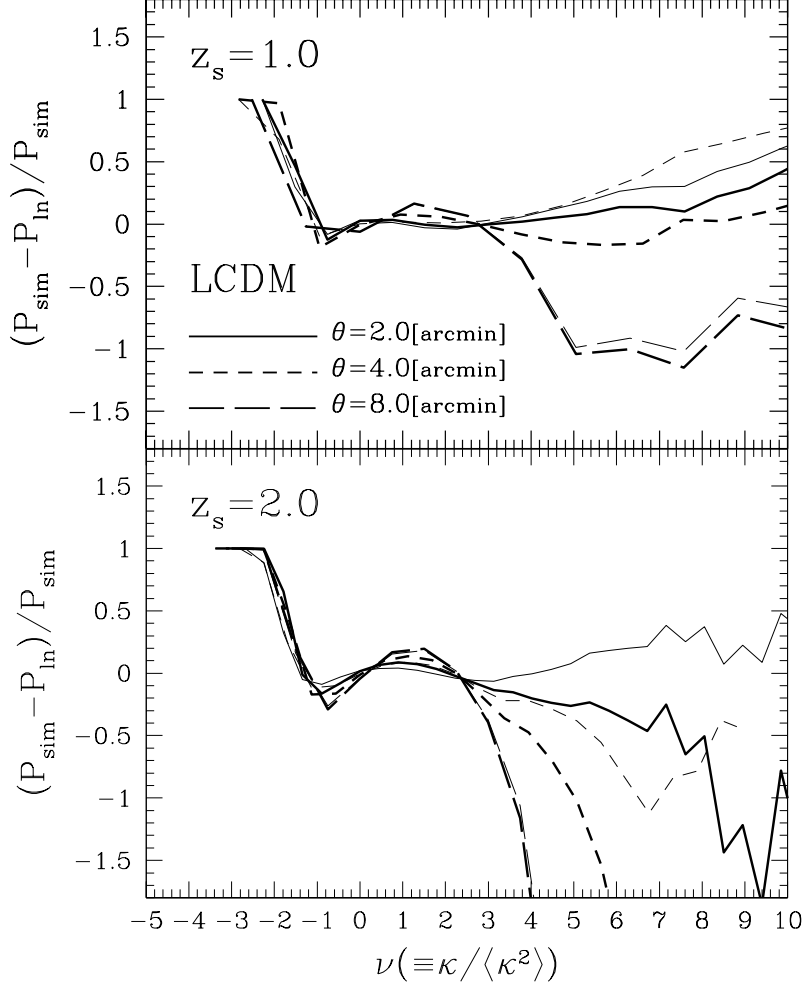


Fig. 5.— Differences of one-point PDFs normalized by the simulated PDF, $[P_{\text{sim}}(\kappa) - P_{\text{in}}(\kappa)]/P_{\text{sim}}(\kappa)$ as a function of level threshold $\nu = \kappa/\langle\kappa^2\rangle^{1/2}$ in LCDM model. Upper(Lower)-panel shows the results fixing the source redshift to $z_s = 1.0$ (2.0). The solid, short-dashed and long-dashed lines represent the cases with smoothing angle $\theta = 2.0'$, $4.0'$ and $8.0'$, respectively. In plotting the ratios, the lognormal prediction adopting the averaged minimum value κ_{min} (see Fig.1) is used in thick lines, while the thin lines represent the results adopting the minimum value of each PDF data.

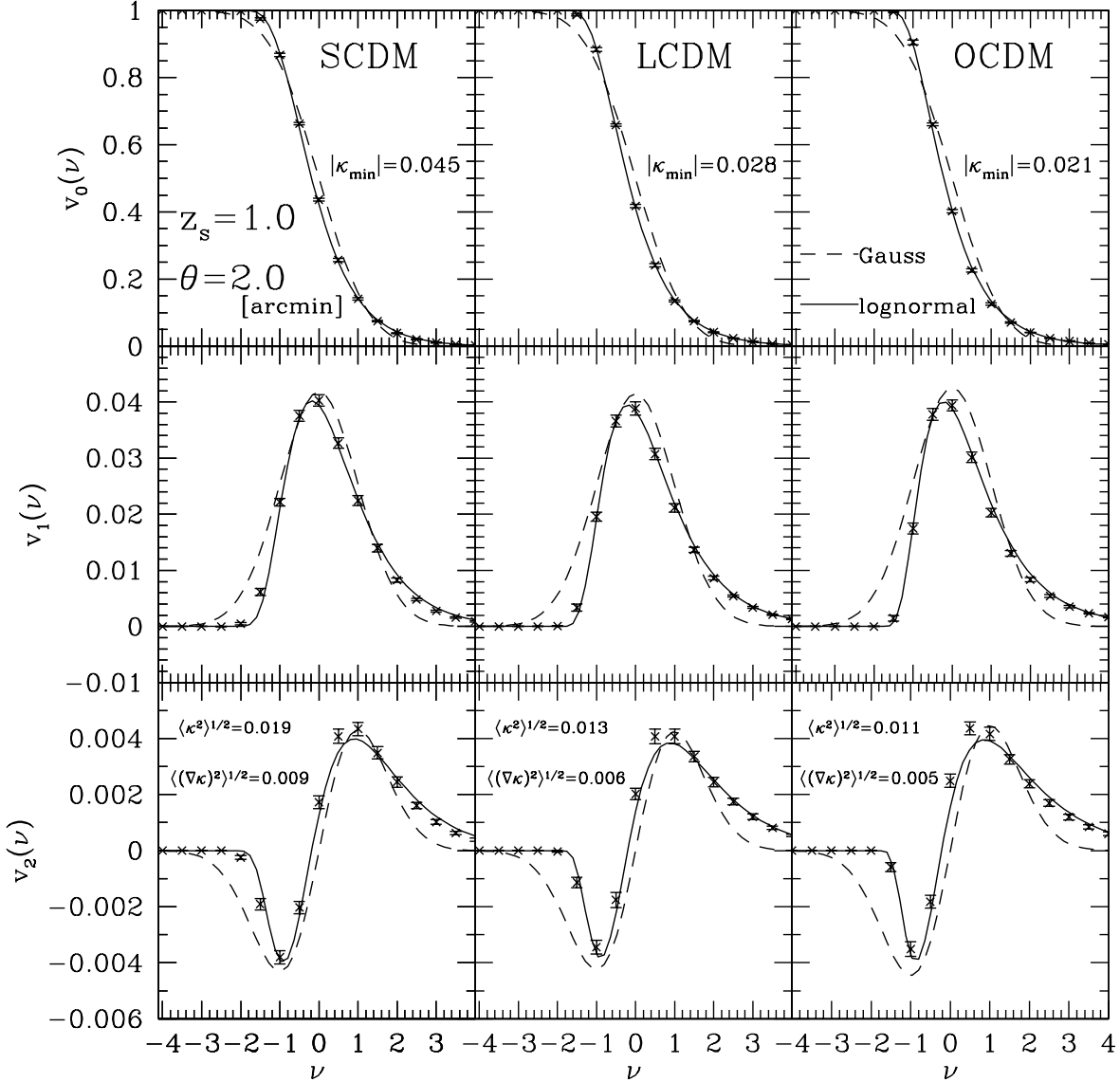


Fig. 6.— Minkowski functionals as a function of level threshold $\nu = \kappa/\langle\kappa^2\rangle$ at the smoothing angle $\theta = 2.0'$. The source redshift is fixed to $z_s = 1.0$. Solid lines show the lognormal predictions based on the formulae (24),(26) and (27), where all the parameters are estimated from simulations. The dashed lines are the Gaussian predictions obtained from (28), (29) and (30): SCDM model (*left*); LCDM model (*middle*); OCDM model (*right*).

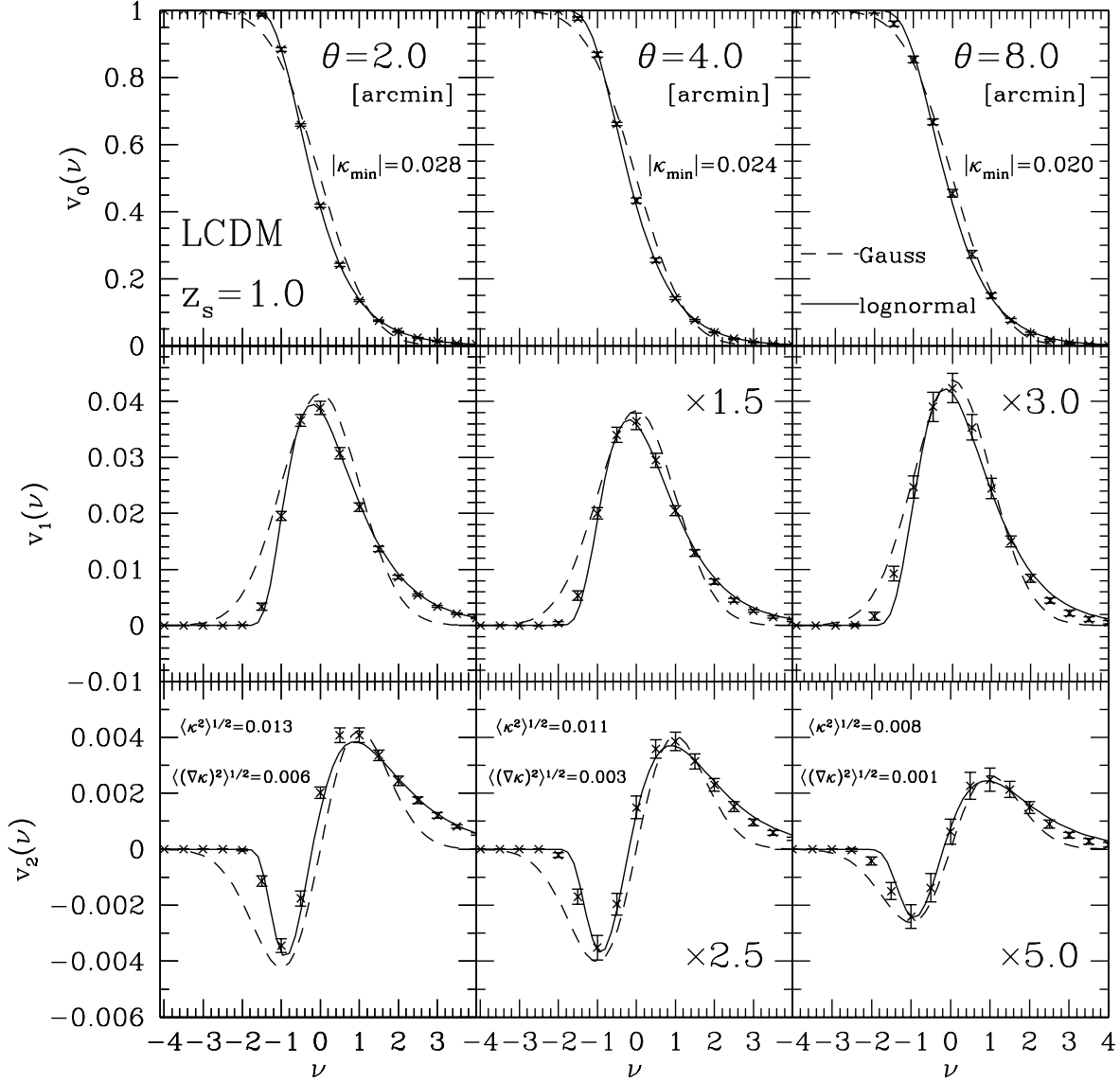


Fig. 7.— Same as Fig.6, but we fix the cosmological model to LCDM model. Here, for illustrative purpose, the amplitude of v_1 and v_2 at the smoothing angle $\theta = 4, 8$ [arcmin] are enhanced in order to clarify the differences as indicated in each panel: $\theta = 2'$ (left); $\theta = 4'$ (middle); $\theta = 8'$ (right).

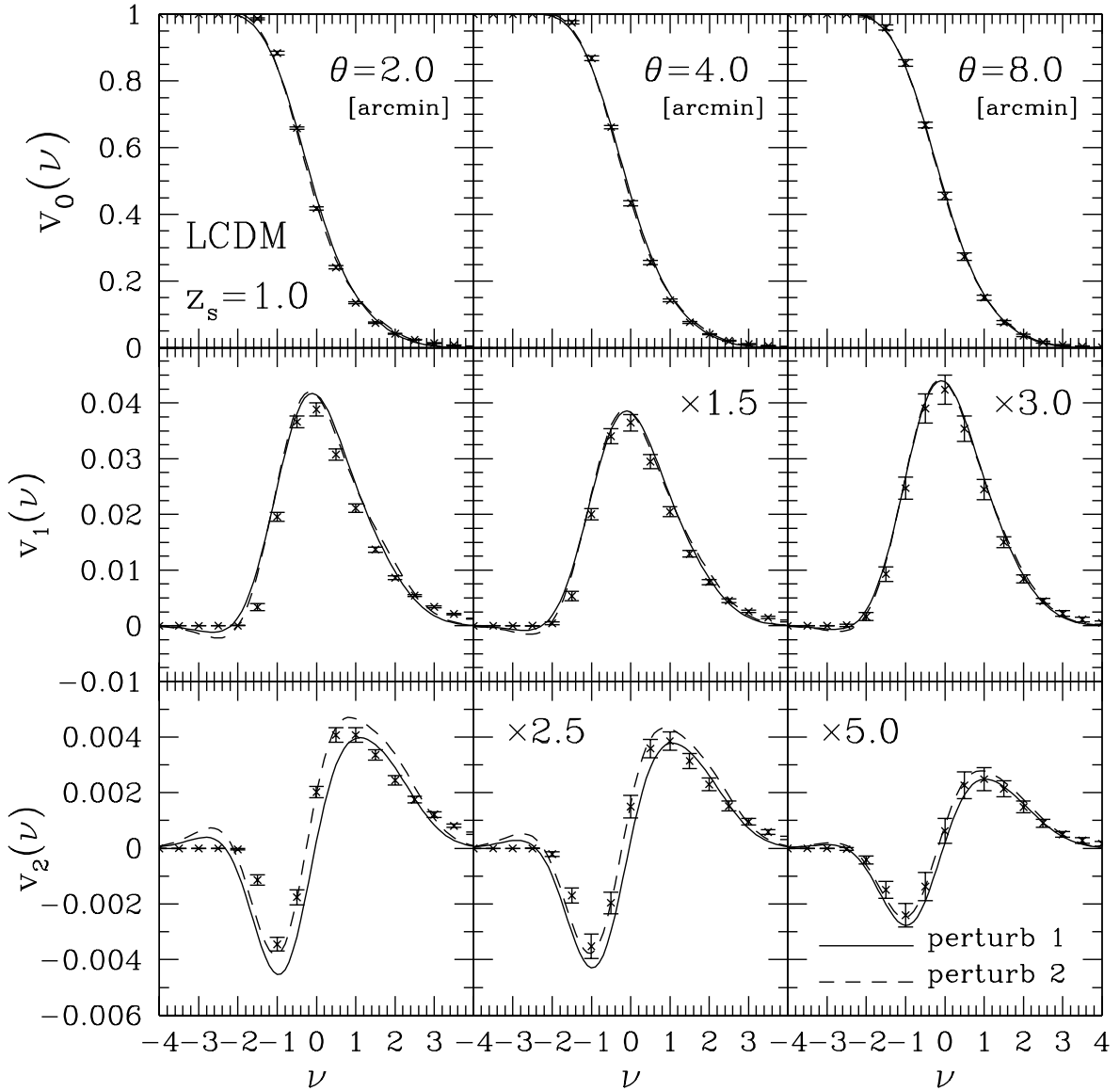


Fig. 8.— Edgeworth expansion of Minkowski functionals compared with the simulations. In each panel, the results of $z_s = 1$ case in LCDM model are shown. Solid lines (*perturb 1*) indicate the perturbation results, where the skewness parameters are calculated via perturbation theory, while the skewness parameters of the dashed lines (*perturb 2*) are estimated from simulation data directly. In plotting both cases, the variances $\langle \kappa^2 \rangle$ and $\langle (\nabla \kappa)^2 \rangle$ are fitted to the numerical simulations. Note that the amplitude of v_1 and v_2 at the smoothing angle $\theta = 4, 8$ [arcmin] are enhanced in order to clarify the differences as indicated in each panel.

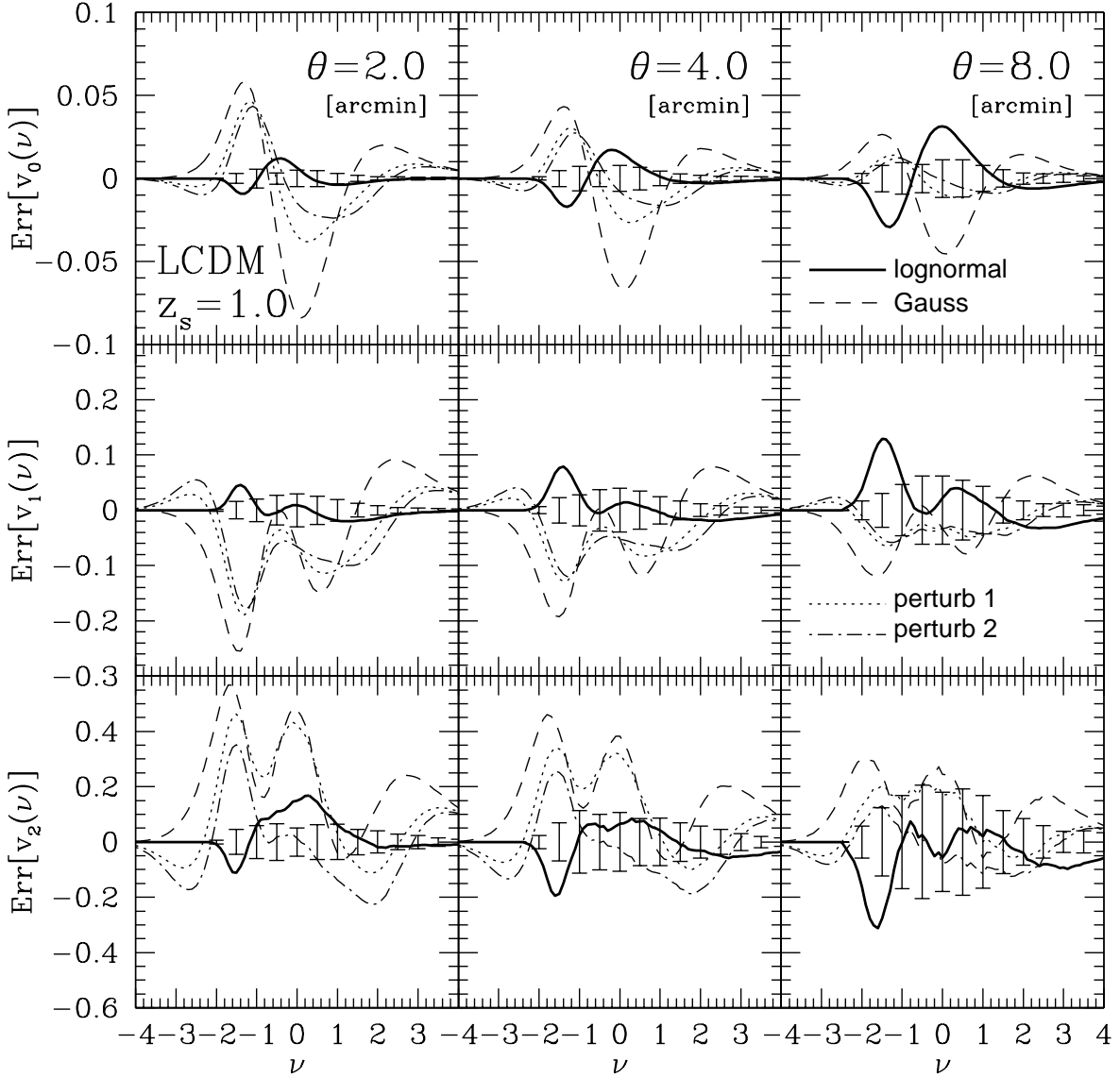


Fig. 9.— Fractional errors of various model predictions in Minkowski functionals, $\text{Err}[v_i(\nu)] \equiv [v_i^{(\text{sim})}(\nu) - v_i^{(\text{model})}(\nu)]/v_{i,\text{max}}^{(\text{sim})}$, in the case of LCDM model with $z_s = 1$. Here, $v_{i,\text{max}}^{(\text{sim})}$ denotes the maximum value of $v_i(\nu)$ estimated from simulation. In each panel, the fractional errors for the lognormal and Gaussian prediction are plotted as thick-solid and dashed lines, respectively. The dotted- and dot-dashed lines represent the perturbative predictions based on the Edgeworth expansion (dotted: *perturb 1*; dot-dashed: *perturb 2*). In each panel, the error-bars around zero mean indicate the realization error of ray-tracing simulations: $\theta = 2'$ (left); $\theta = 4'$ (middle); $\theta = 8'$ (right).

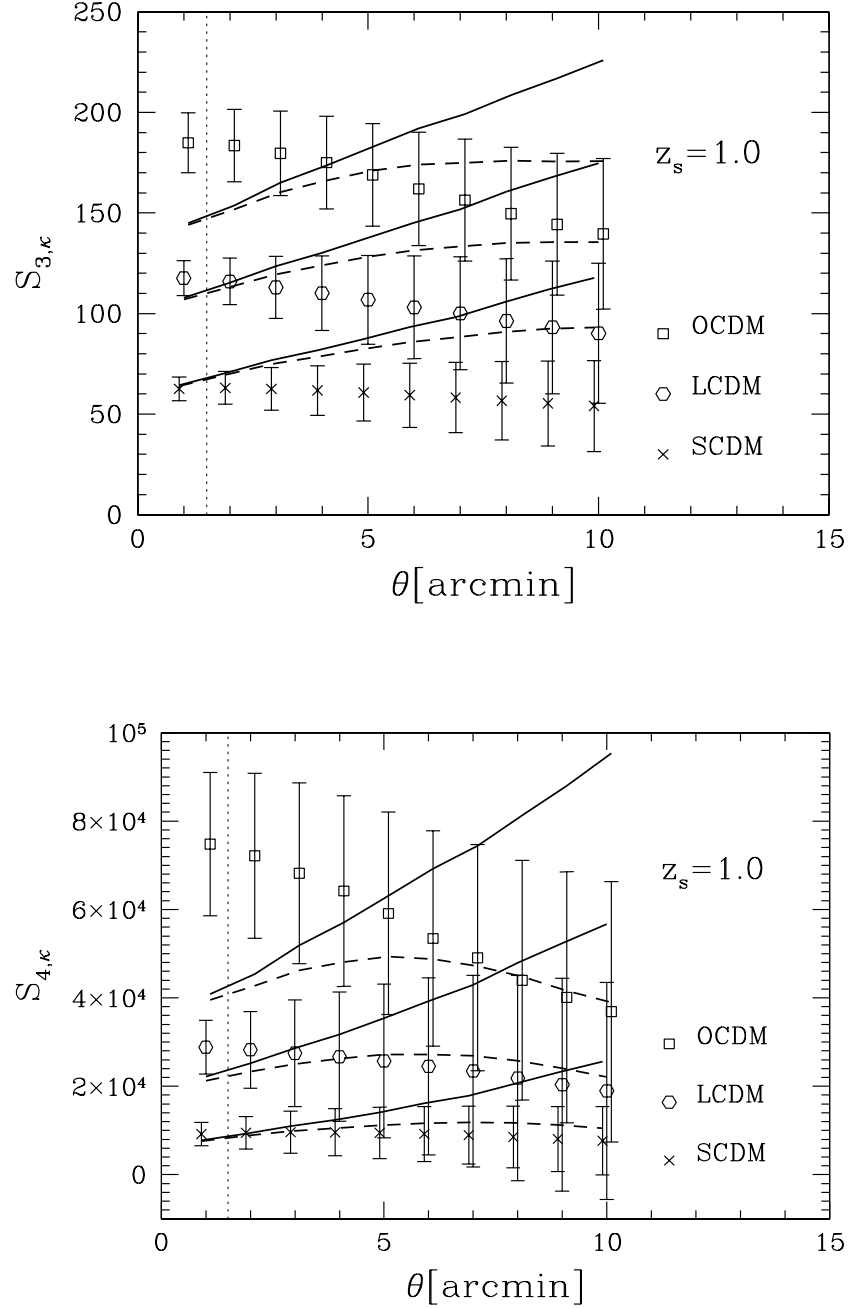


Fig. 10.— Skewness $S_{3,\kappa}$ (*upper*) and kurtosis $S_{4,\kappa}$ (*lower*) as a function of smoothing angle. The crosses, hexagons and squares with error-bars represent the simulation results in SCDM, LCDM and Λ CDM, respectively. The solid lines show the lognormal prediction based on the expressions, (39) and (40). The dashed lines also indicate the lognormal prediction, but here we take into account the limited range of convergence data, i.e., $\kappa_{\min} < \kappa < \kappa_{\max}$.